RSC Advances

PAPER

View Article Online
View Journal | View Issue



Cite this: *RSC Adv.*, 2026, **16**, 17555

# Empowering solar-driven degradation: advancements in lanthanum-doped $Bi_2O_3$/g-$C_3N_4$ heterojunctions for high-performance photocatalysis

M. M. Rashed,[a] Mohamed Abdel Rafea,[a] Mohamed I. Attia,[b] Mohamed R. El-Aassar,[c] Tasneem I. Hussein,[d] Salma Saddeek,[e] Imran Shakir,[f] Mazen R. Alrahili[g] and Muhammad Aadil *[h]

The lanthanum-doped bismuth oxide (La-$Bi_2O_3$) anchored g-$C_3N_4$ (g-CN) heterojunction-based photocatalyst (La-$Bi_2O_3$/g-CN) has been designed with visible-light activation and prompt interfacial charge transfer. Pure and La-doped bismuth oxide nanomaterials were prepared *via* a hydrothermal method, while g-CN was obtained by thermal polymerization of melamine. The doped material was anchored over the 2D g-CN to make the heterojunction (Type-II) by prolonged ultrasonication. As-synthesized samples were characterized *via* XRD, FT-IR, TGA, SEM, TEM, UV-vis, PL spectroscopy, Mott–Schottky plots, EIS, and photocurrent response to investigate the structural features, thermal endurance, topography, optical response, and interfacial charge mobility. The photocatalyst's efficiency was determined by degrading methylene blue (MB) and ciprofloxacin (CPF) as representative pollutants under visible-light irradiation. The heterojunction material displayed promising photocatalytic activity compared to its pure counterparts and photodegraded 97% of MB and 84% of CPF, following 1st-order kinetics. This remarkable efficiency was due to the band structure tuning of bismuth oxide by La-doping and architecting heterojunction La-$Bi_2O_3$/g-CN with g-CN, which promotes the interfacial charge transfer, delaying recombination of the separated charges. The scavenging results revealed that the hydroxide radicals ($HO^{\bullet}$) and holes ($h^+$) correspondingly facilitated the MB and CPF degradation.

Received 19th February 2026
Accepted 24th March 2026

DOI: 10.1039/d6ra01451h

rsc.li/rsc-advances



## 1. Introduction

The demand for the development of sustainable technologies for clean energy production and environmental pollution control has sparked substantial interest in visible-light responsive photocatalysis, a process involving a semiconductor material to drive the chemical reaction, presenting a promising approach to these overwhelming challenges.[1] The efficiency of a photocatalyst significantly hinges on several factors, including light absorption, electron–hole pair generation, and interfacial charge transfer (delaying charge carriers' recombination) to generate the reactive oxygen species.[2,3] The materials, including oxides (ZnO,[4] $TiO_2$,[5] $Fe_2O_3$,[6] $WO_3$,[7] $Bi_2O_3$,[8] $MoO_3$,[9] $SnO_2$,[10] and $V_2O_5$ (ref. 11)), sulfides (CdS,[12] $MoS_2$,[13], ZnS,[14] $Bi_2S_3$,[15] and $In_2S_3$ (ref. 16)), selenides (CdSe[17] and ZnSe[18]), and carbonaceous materials,[19] have been explored as photocatalysts. The wide energy bandgaps of the semiconductors limit their visible light absorption, rendering them ineffective and restricting solar light harvesting.[20,21] Another key limitation is the rapid recombination of photogenerated $e^-$–$h^+$ pairs, which hampers the redox reaction to generate the reactive oxygen species.[22–24] Therefore, designing photocatalysts that are visible-light-responsive with enhanced charge separation is crucial to improve their efficiency.

Bismuth oxide $Bi_2O_3$, a semiconductor with thermal and chemical stability, is a promising material for visible-light-responsive photocatalysis as it features resistance to photocorrosion.[25,26] The band structure of $Bi_2O_3$ includes Bi 6s and O 2p hybrid orbitals in the valence-band maxima and Bi 6p orbitals in the conduction-band minima, which support the

[a]*Department of Physics, College of Science, Imam Mohammad Ibn Saud Islamic University (IMSIU), 11623, Riyadh, Saudi Arabia*
[b]*Department of Chemistry, College of Science, Imam Mohammad Ibn Saud Islamic University (IMSIU), 11623, Riyadh, Saudi Arabia*
[c]*Chemistry Department, College of Science, Jouf University, Sakaka, 2014, Saudi Arabia*
[d]*Department of Chemistry, College of Science, Qassim University, Buraydah, 51452, Saudi Arabia*
[e]*Department of Chemistry, Faculty of Sciences, University of Hafr Al Batin, Hafr Al Batin 39524, Saudi Arabia*
[f]*Department of Physics, Faculty of Science, Islamic University of Madinah, Madinah 42351, Saudi Arabia*
[g]*Department of Physics, College of Science, Taibah University, Madinah, Saudi Arabia*
[h]*Department of Chemistry, The Islamia University of Bahawalpur, Rahim Yar Khan Campus, Rahim Yar Khan 64200, Pakistan. E-mail: Muhammad.aadil@iub.edu.pk*

visible light absorption resulting in photoexcitation.[27–29] Nevertheless, the rapid recombination of these charge carriers severely compromises their photocatalytic efficiency. Therefore, the band structure modification to reduce the fast recombination is crucial to designing bismuth oxide-based photocatalysts.[30] Graphitic carbon nitride, a metal-free semiconductor, is a sustainable option for photocatalytic applications. Still, its practical applicability needs further optimization, as its photocatalytic activity is hindered by limited light response and rapid charge-carrier coupling.[31,32] Various investigations have revealed that using g-CN for designing composite-based photocatalysts is a practical approach that tunes the overall catalytic activity of the g-CN-derived material under solar light exposure.[33–35] Composite materials with an active heterojunction architecture exhibit properties tuned for photocatalytic applications, including increased light absorption and efficient charge transfer.[36,37]

In light of the facts mentioned above, we have designed a heterojunction (Type-II) material by anchoring lanthanum-doped bismuth oxide on the 2D graphitic carbon nitride (g-CN) with visible-light activation and prompt interfacial charge transfer for solar light harvesting to derive potential photocatalytic applications. Initially, pure bismuth oxide (abbreviated as BO) and its La-doped counterpart (abbreviated as LBO) were hydrothermally fabricated, while the calcination of melamine synthesized g-CN *via* thermal polymerization. Afterward, using the ultrasonication approach, the doped LBO material was loaded on the g-CN to architect the LBO/g-CN heterojunction. Physicochemical and opto-electro investigations were performed to prove the nature of the material and validate its suitability for efficient photocatalysis. MB and CPF were degraded as representative organic pollutants over the synthesized photocatalysts to evaluate their catalytic efficiency. The degradation reaction kinetics, reactive oxygen species tracking, and reusability of the heterojunction LBO/g-CN photocatalyst were explored to gain insights into the potential applicability of the designed photocatalyst.

## 2. Experimental

### 2.1 Chemicals

The analytical grade precursors were used for the preparation of pure and lanthanum-doped bismuth oxide nanomaterials, which include lanthanum(III) nitrate hexahydrate ($La(NO_3)_3 \cdot 6H_2O$, Sigma-Aldrich, ≥99.99%) and bismuth(III) nitrate pentahydrate ($Bi(NO_3)_3 \cdot 5H_2O$, Sigma-Aldrich, ≥99.99%). Melamine ($C_3H_6N_6$, 99%, Sigma-Aldrich) was used to prepare g-CN. In contrast, MB ($C_{16}H_{18}ClN_3S$, ≥82%, Sigma-Aldrich) and CPF ($C_{17}H_{18}FN_3O_3$, Sigma-Aldrich, ≥98%) were used as representative organic pollutants for investigating the photocatalytic activity of the designed photocatalysts. For the scavenging experiment, isopropyl alcohol (IPA, 99.9%), benzoquinone (BQ, 99%), and ethylenediaminetetraacetic disodium salt (EDTA-2Na, 99%) were used to quench the reactive oxygen species (ROS) generated during MB and CPF degradation.


Fig. 1 Schematic presentation of BO, LBO, g-CN, and LBO/g-CN synthesis.

### 2.2 BO and LBO nanomaterials synthesis

The pure and La-doped nanomaterials, BO and LBO, were synthesized *via* the hydrothermal approach. The bismuth precursor ($Bi(NO_3)_3 \cdot 5H_2O$) was dissolved in DI water by magnetic stirring, followed by the addition of a lanthanum precursor ($La(NO_3)_3 \cdot 6H_2O$) for doped counterpart preparation. The solution was stirred (300 rpm) until complete dissolution of precursor salts, and then the $NH_4OH$ was gradually added to raise the pH to ~9. Afterward, the final remedy was charged into a stainless-steel autoclave (Internally Teflon-lined) and heated for 12 hours at 180 °C. The synthesized nanomaterial was thoroughly rinsed with water to wash off the residuals and dried at 60 °C.

### 2.3 Powder g-CN synthesis

The g-CN was fabricated through the thermal condensation of melamine.[38] Experimentally, 5 grams of the melamine powder was transferred into the lidded crucible and introduced into a furnace, followed by calcination at 550 °C with a heating rate of 10 °C $min^{-1}$ for 6 hours to polymerize melamine, forming 2D hexagonal rings of carbon and nitrogen network. The canary-yellowish-coloured g-CN formed was stored in a moisture-free environment.

### 2.4 Fabrication of LBO/g-CN heterojunction

The La-doped nanomaterial LBO was loaded onto the synthesized g-CN sheets to architect the LBO/g-CN heterojunction by ultrasonication. Initially, 460 mg of the LBO and 40 mg of the g-CN were dispersed in DI water in separate beakers by magnetic stirring (500 rpm), followed by sonication in the ultrasonic bath (40 kHz) for $\frac{1}{2}$ hour at ambient temperature. The suspensions mentioned above were poured into a beaker, and the resultant blend was ultrasonicated for 60 minutes. The composite formed was separated by centrifugation (300 rpm) and dried in the oven (vacuum, 60 °C, 6 hours) to get the designed heterojunction in a ratio of 9 : 1 of LBO to g-CN. The preparation scheme of BO, LBO, g-CN, and LBO/g-CN materials is shown Fig. 1.

### 2.5 Photocatalytic activity (PCA)

The PCA of the designed BO, LBO, and LBO/g-CN was determined by photocatalytic MB and CPF degradation as model dyestuff and antibiotic organic pollutants. Initially, 0.05 g of the catalysts (BO, LBO, and LBO/g-CN) were separately dispersed in 100 mL (20 mg $L^{-1}$) of the contaminants (MB and CPF) solutions. These suspensions containing the catalysts were kept in

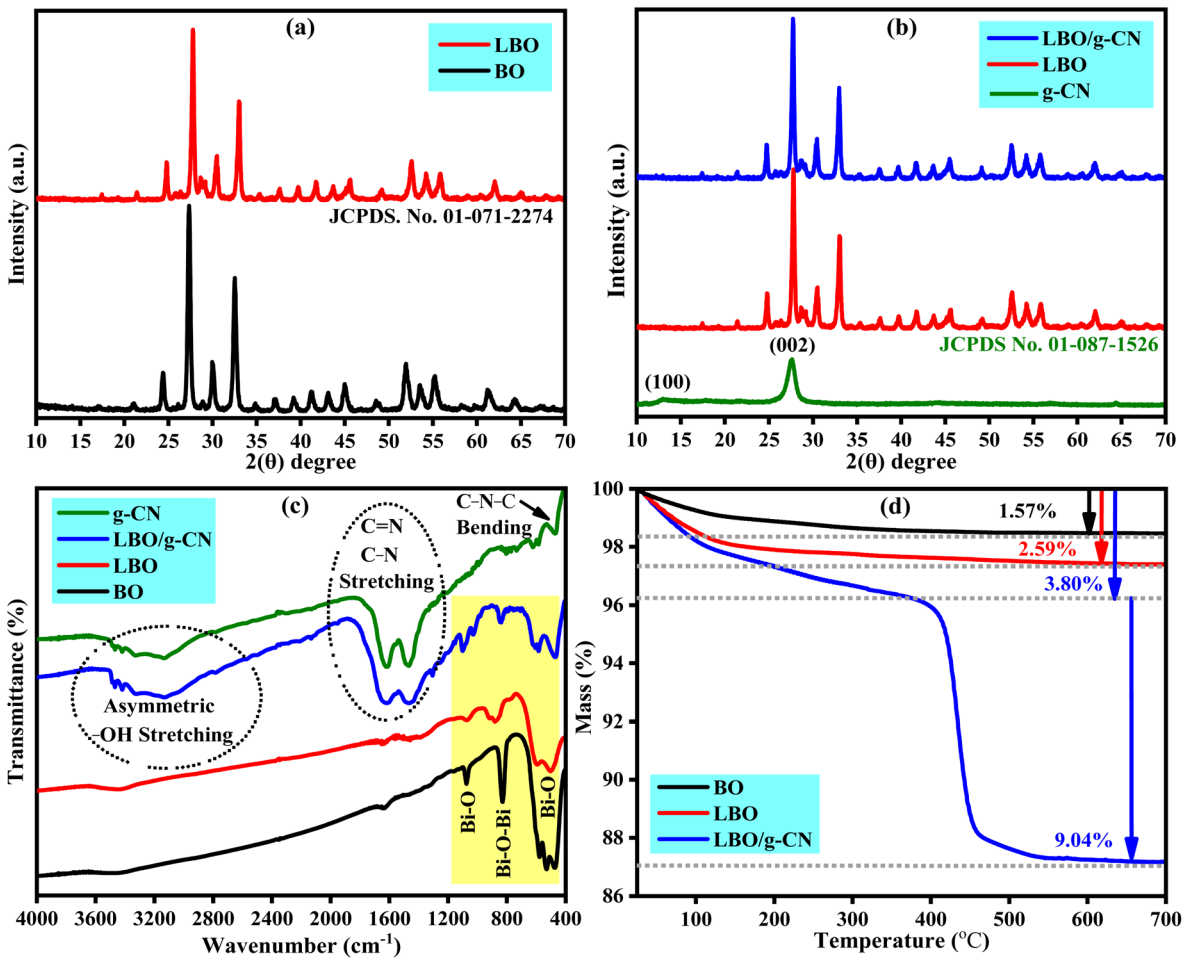


Fig. 2 (a and b) Diffraction patterns of the designed BO, LBO, g-CN, and LBO/g-CN, (c) FT-IR spectra displaying characteristic vibrations, and (d) TGA curves showcasing the thermal stability of the catalysts.

the dark while stirring for adsorption–desorption of pollutant at the catalyst surface. After about 30 minutes, the aliquots were exposed to visible light (Xe lamp, 300 W) to start the photocatalytic degradation of MB and CPF. The small portion from the degrading mixtures was separated at regular time intervals, and the absorbance of the sample drawn was monitored to estimate the concentration of pollutants. The efficiency of the photocatalysts was estimated by calculating the degradation (%) by applying eqn (1), while for the kinetics study of MB and CPF degradation, eqn (2) was applied. The scavenging investigation was performed by adding quenchers, including IPA, EDTA-2Na, and BQ, to the photocatalyst LBO/g-CN.

$$\text{Degradation}(\%) = 1 - \frac{C_t}{C_o} \quad (1)$$

$$-\ln\frac{C_t}{C_o} = Kt \quad (2)$$

# 3. Results and discussion

## 3.1 Structural characteristics and thermal stability

The synthesized materials' phase formation, purity, and crystallite size were determined from their XRD patterns, which are displayed in Fig. 2(a and b). The Bragg's diffraction at $2\theta$ = 21.10°, 34.36°, 32.58°, 34.10°, 37.03°, 39.26°, 41.14°, 43.20°, 44.91°, 48.68°, 51.93°, 53.64°, 55.19°, 61.18°, and 64.26° corresponds to the (020), (−102), (−211), (−212), (−131), (−222), (−213), (−123), (023), (−232), (−104), (−313), (−224), (232), (−115) crystallographic planes and coincided with the JCPDS No. 01-071-2274 in good agreement, confirming the formation of the designed monoclinic $Bi_2O_3$ phase ($P2_1/c$).[39] The sharp and narrow peaks in the diffraction patterns of the BO, LBO, and LBO/g-CN materials define the well-crystalline nature of these materials. The peaks at $2(\theta)$ values of 12.91° and 27.54° in the diffraction profile of g-CN correspond to the (100) and (200) crystallographic planes (JCPDS No. 01-087-1527).[40] The slight variation of peak positions and intensity after La-doping and

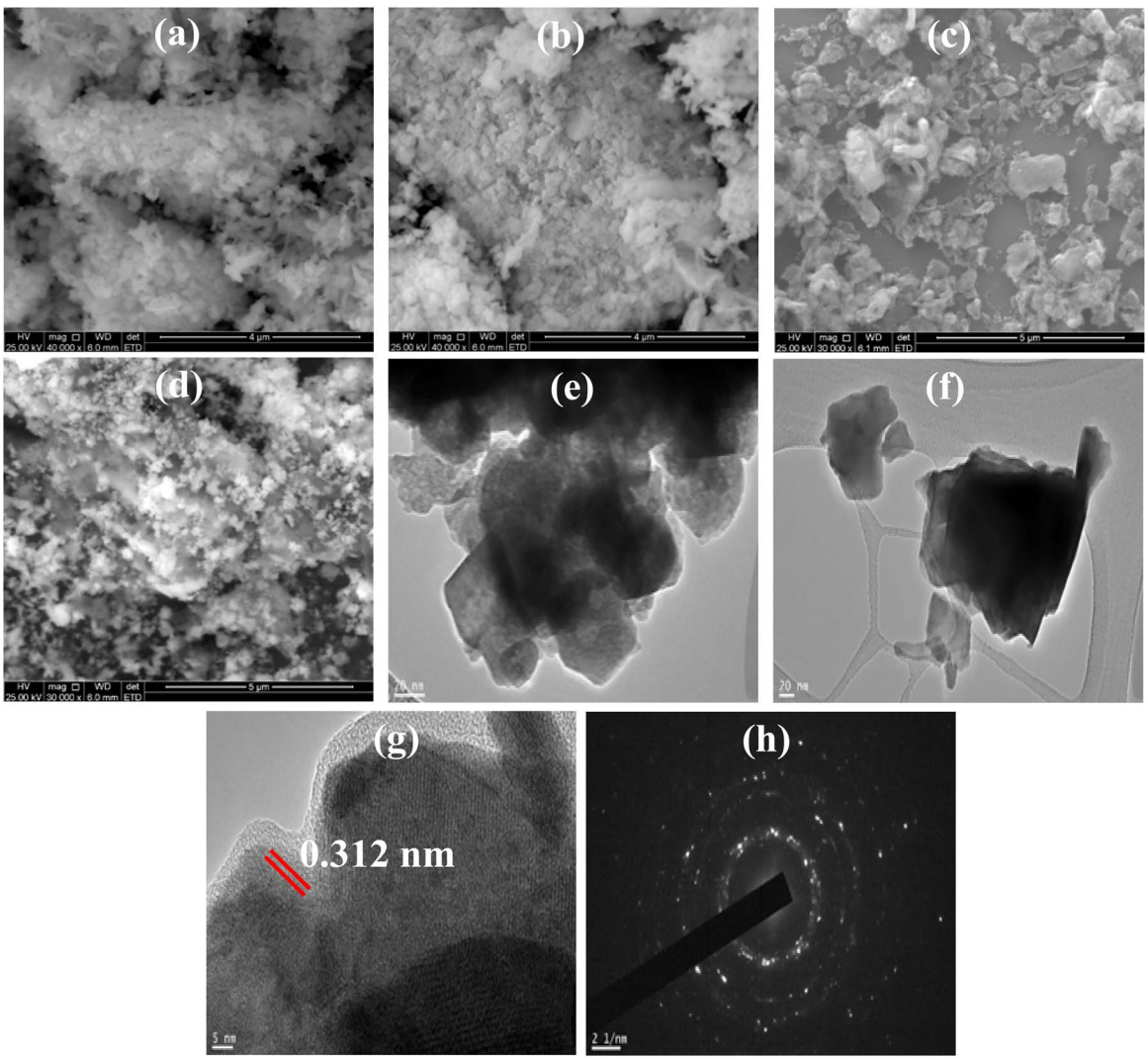


Fig. 3 SEM images of (a) BO, (b) LBO, (c) g-CN, and (d) LBO/g-CN, and TEM images of (e) LBO/g-CN, (f) g-CN, and (g and h) HRTEM and SAED pattern of LBO/g-CN.

anchoring doped material on g-CN reflects a change in crystallographic characteristics, primarily due to structural deformation leading to defective regions.[41–43] The average crystallite sizes (calculated by applying Scherrer's formula $D = 0.9\lambda/\beta \cos\theta$ (ref. 44)) of BO, LBO, and LBO/g-CN were 24.41 nm, 26.31 nm, and 29.45 nm, respectively, which is possibly due to lattice strain relaxation, which facilitates the crystallite growth.[45]

The functional properties of the synthesized materials with characteristic metal–oxygen vibrations were confirmed by FT-IR spectra, as displayed in Fig. 2(c). The characteristic Bi–O stretching (~1077 $cm^{-1}$), Bi–O–Bi stretching (~830 $cm^{-1}$), and Bi–O bending (~522 $cm^{-1}$) in the fingerprint region confirm the formation of the designed material.[46–48] In the FT-IR pattern of the synthesized g-CN, the C=N stretching (~1623 $cm^{-1}$), C–N stretching (~1469 $cm^{-1}$), and C–N–C bending (~481 $cm^{-1}$) are typical peaks of g-CN, confirming its synthesis.[49,50] The wide band in the high-frequency range (3200–3600 $cm^{-1}$) is owing to –OH stretching and appeared due to adsorbed moisture.[51,52] The decrease in vibrational peak intensity of g-CN in LBO/g-CN, in contrast to its pure counterpart, confirms the interaction between these two materials forming LBO/g-CN heterostructures.[53]

The TAG profiles of BO, LBO, and LBO/g-CN are displayed in Fig. 2(d). The insignificant mass loss of 1.57% and 2.59% for BO and LBO materials was due to moisture removal, confirming the phase stability of the materials. For the LBO/g-CN heterojunction architect, mass loss in two temperature zones was observed. The first mass loss (3.80%) was due to the removal of adsorbed moisture, while the second mass loss (9.04%) in the temperature range of 400–600 °C was carbon content combustion of g-CN.[54] The mass loss observed for the g-CN removal was much closer to the amount used for LBO/g-CN architecting.

### 3.2 Morphological study

The SEM and TEM images of as-synthesized BO, LBO, g-CN, and LBO/g-CN are presented in Fig. 3. The pure bismuth oxide exhibits dispersion of irregular-sized microcrystallites featuring irregular symmetry. La-doping affected the overall size of crystallites, but the irregularity of size and symmetry was retained, as evidenced by the SEM image of the LBO material. The synthesized g-CN features dispersed flakes that have an irregular shape. In contrast, by forming a composite with LBO to architect the LBO/g-CN heterojunction, the g-CN flakes were

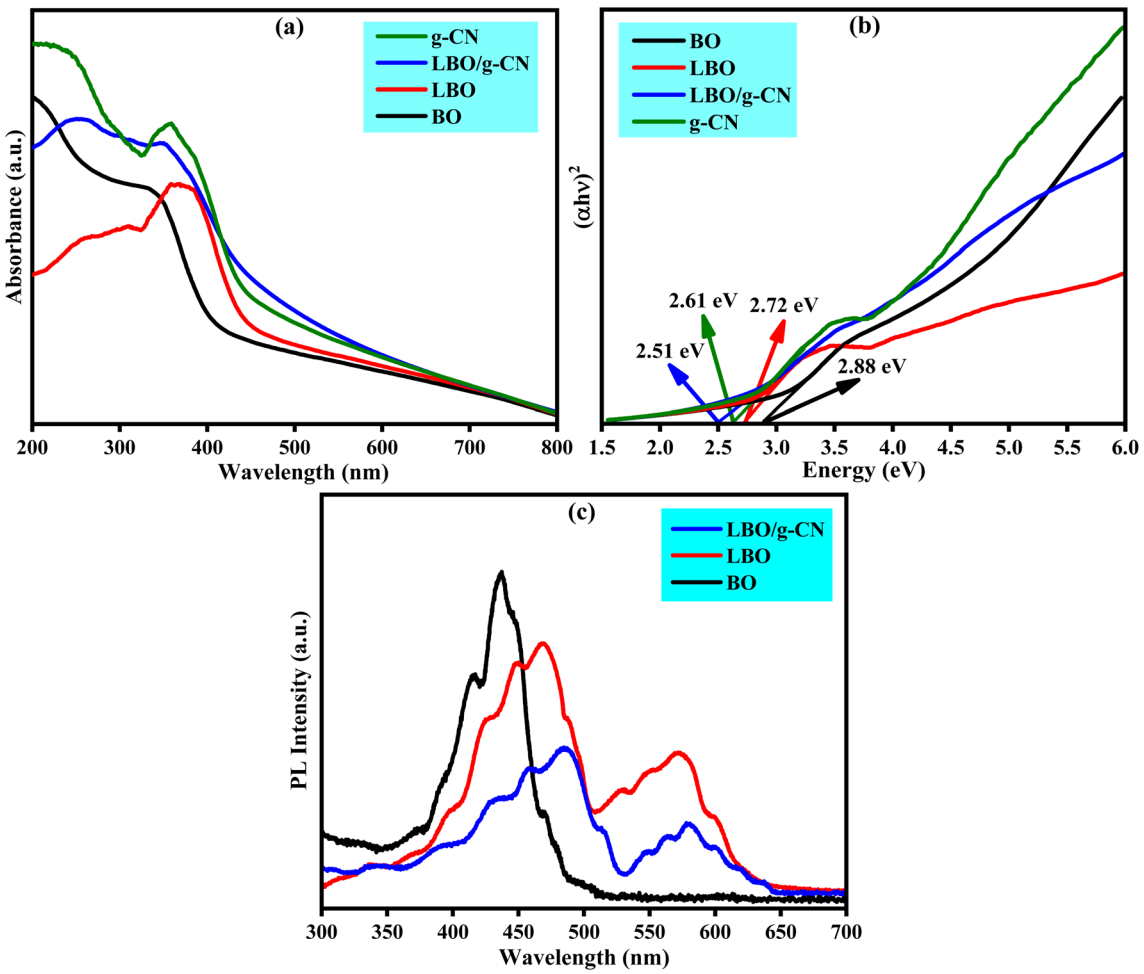


Fig. 4 (a) Absorption (200–800 nm) spectra of BO, LBO, g-CN, and LBO/g-CN, (b) Tauc plots displaying the optical bandgaps, and (c) PL spectra of the catalysts.

covered with the dispersion of LBO crystallites, representing the uniformity of the composite. This dispersion will facilitate the interfacial charge transfer by delaying the possible charge recombination, which is promising for photocatalytic activity.[55] The TEM images of pure g-CN and LBO/g-CN heterojunction materials are displayed in Fig. 3(e and f). The LBO material is a hybrid with g-CN flakes that have a crystalline nature. The lattice fringes feature an interplanar spacing of 0.312 nm corresponding to the (−102) plane, as showcased in the HRTEM image of LBO/g-CN.

### 3.3 Optical properties

The optical activity, which plays a substantial role in visible-light-driven catalytic activity, was investigated by recording the absorption ($\lambda$ = 200–800 nm) of the designed BO, LBO, g-CN, and LBO/g-CN materials, and the absorption spectra are displayed in Fig. 4(a). The pure BO material shows an absorption edge near the start of the visible light region, which is red-shifted by La-doping, as can be evident from the absorption of LBO material. This shift is exhibited due to band structure deformation by generating sub-states within the valence and conduction bands, which triggers visible light activation.[56,57] The pure g-CN displays visible light activation, which was further increased by anchoring the LBO material. In contrast to its pure counterparts, the assembled heterojunction LBO/g-CN with enhanced visible light activity could be a potential photocatalyst for visible light harvesting. The optical energy ($E_g$) gap was determined by the Tauc plot equation (Fig. 4(b)), and its values were 2.88 eV, 2.72 eV, 2.61 eV, and 2.51 eV for BO, LBO, g-CN, and LBO/g-CN. The decline in $E_g$ can be credited to an active heterojunction architecture with the conduction of separated charges, which is promising for solar-driven applications.[58,59] The suppression of the charge recombination phenomenon was studied by the PL spectroscopic analysis, and the results are depicted in Fig. 4(c). The radiant decay was of high intensity for the pure BO material, which highlights the rapid recombination that was delayed by La-doping and suppressed significantly by the heterojunction LBO/g-CN formation as the PL intensity declines after modifications. The heterojunction construction prevents the recombination by spatial separation of the charge carriers, where the negative electrons move to the semiconductor with a lower conduction band and the positive holes

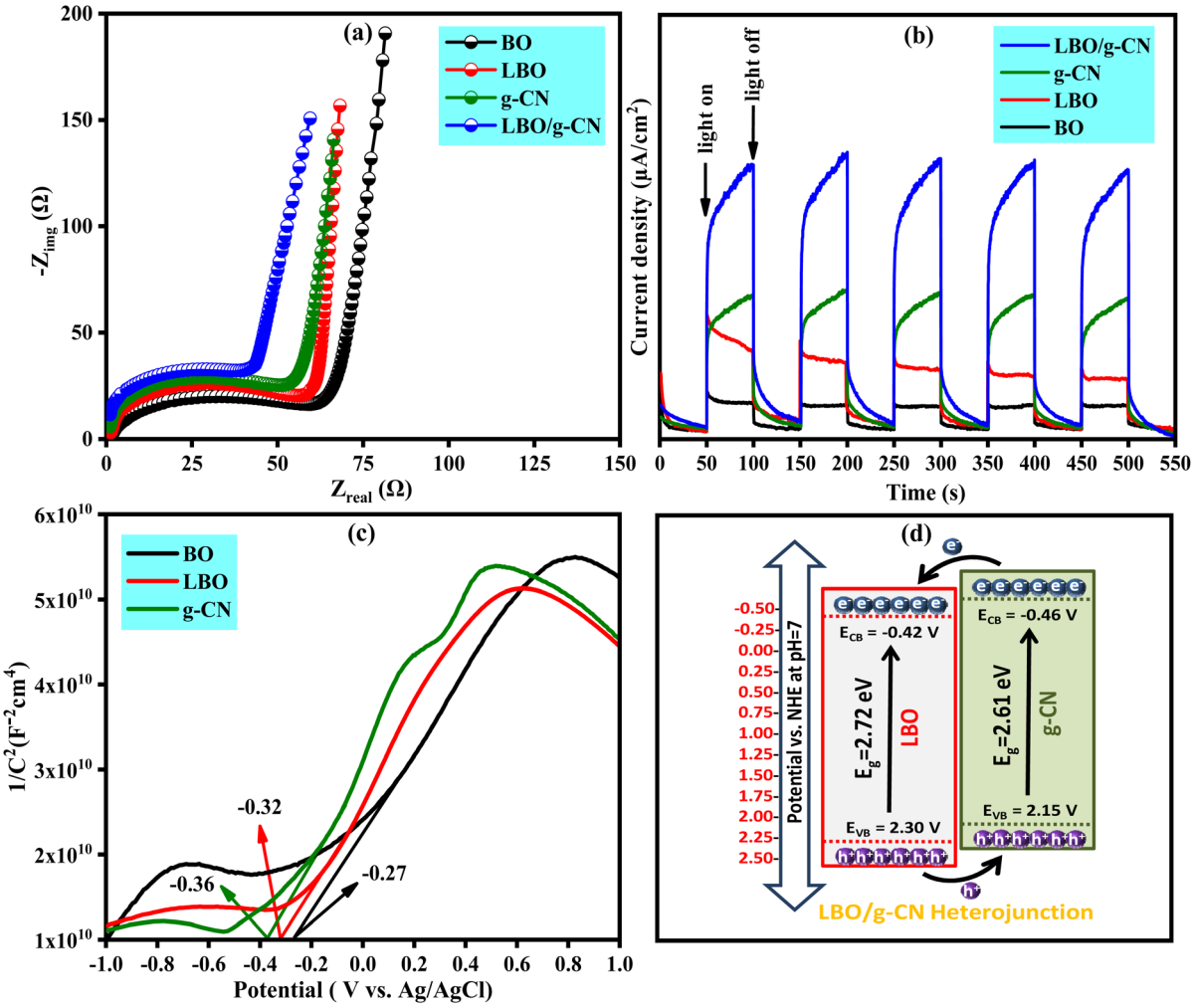


Fig. 5 (a) EIS Nyquist plots, (b) photocurrent response during light-on light-off cycles, (c) Mott–Schottky plots, and (d) schematic display of the designed LBO/g-CN heterojunction (Type-II).

to the semiconductor with a higher valence band, preventing their fast recombination.[60]

### 3.4 Electrochemical properties

The as-designed materials BO, LBO, and LBO/g-CN were subjected to electrochemical characterizations, including EIS, photocurrent response, and Mott–Schottky analysis, to get insights into the charge transfer characteristics, which significantly drive photocatalytic performance. The electrochemical measurements were performed using modified indium-tin-oxide ITO glass, ITO–BO, ITO–LBO, ITO–g-CN, and ITO–LBO/g-CN as working electrodes on a three-electrode potentiostat. The auxiliary and reference electrodes were a Pt-plate and Ag/AgCl in 1 M $Na_2SO_4$ electrolyte. The Nyquist plots for BO, LBO, g-CN, and LBO/g-CN materials are featured in Fig. 5(a). The Nyquist semicircle arc radii are inversely proportional to the material's interfacial charge (electron) transfer.[61] The smaller Nyquist radii for the LBO/g-CN heterojunction indicate a higher electrode reaction rate, reflecting lower charge transfer resistance at the photocatalyst–electrolyte interface due to a more rapid interface electron transfer.[62]

The photocurrent response was recorded under a visible-light source to explore the dynamics of charge separation and transfer, and the photocurrent generated during light-on and light-off cycles for the sample BO, LBO, g-CN, and LBO/g-CN materials is displayed in Fig. 5(b). The greater photocurrent intensity for the LBO/g-CN heterojunction, in contrast to the BO, LBO, and g-CN, showcases higher charge separation and transfer due to the low recombination rate of the charge carriers.[63,64] The results reveal prompt interfacial charge separation and transfer for the architected LBO/g-CN heterojunction, which are promising for photocatalytic activity.

The Mott–Schottky analysis revealed the semiconductor nature and the synthesized materials' band structure. The Mott–Schottky plots generated for the BO, LBO, g-CN, and LBO/g-CN are displayed in Fig. 5(c). The tangents drawn to the linear part of the curves at the horizontal axis exhibit a positive slope, which features n-type semiconductor formation.[65] The flat-band potentials ($E_{fb}$) of BO, LBO, and g-CN were determined to be −0.27 V, −0.32 V, and −0.36 V, respectively. The $E_{fb}$ is almost equal to the Fermi level for n-type semiconductors, and its conduction band potential ($E_{CB}$) is generally 0.1 V more negative than its $E_{fb}$.[66] Following this general agreement, $E_{CB} = E_{fb} - 0.1$, the $E_{CB}$ of the LBO and g-CN are −0.42 V and −0.46 V, while their $E_{VB}$ was determined by using the relation $E_{VB} = E_{CB} + E_g$, where $E_g$ is the optical energy bandgap value.[67,68] The $E_{VB}$ was

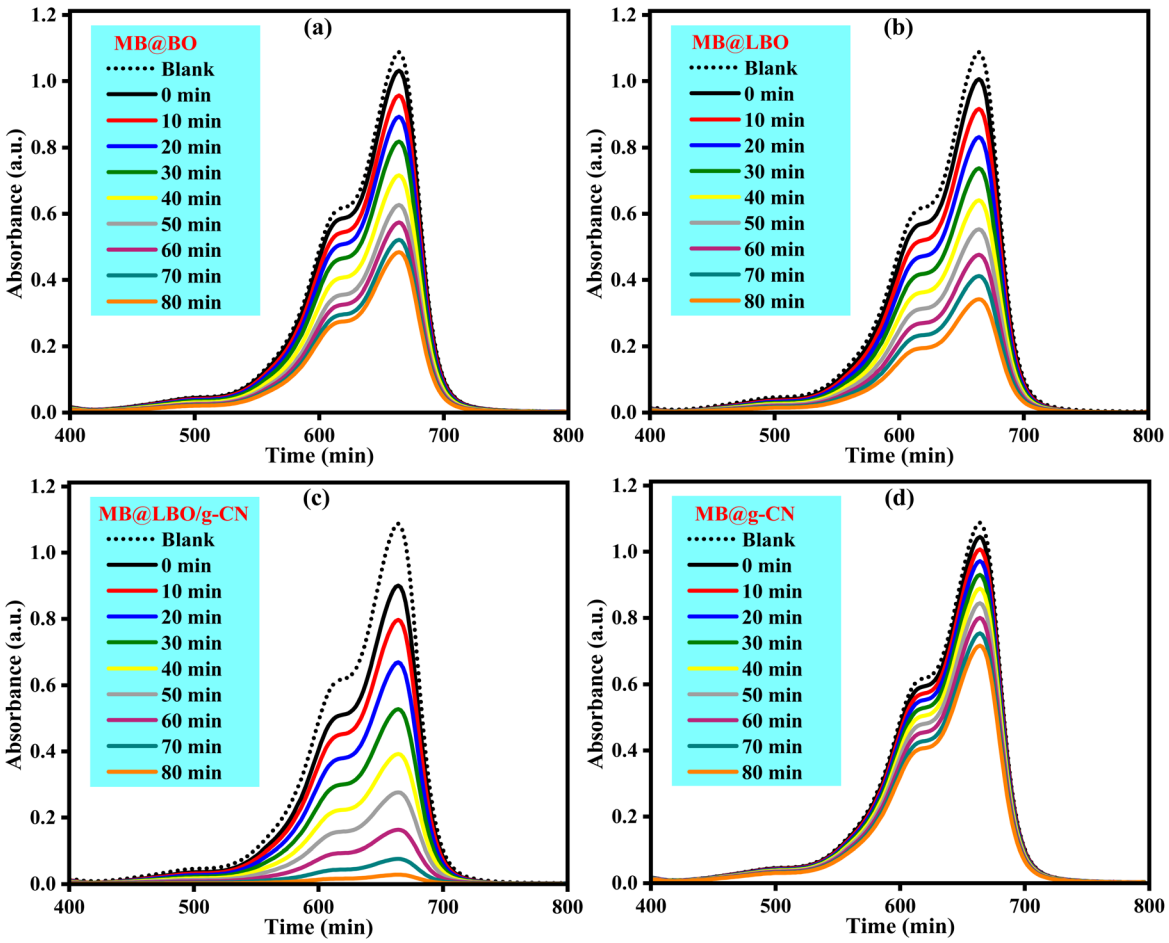


Fig. 6 UV-vis absorption (overlaid) of the samples separated from the aliquot during MB photodegradation over defined time intervals in the presence of (a) BO, (b) LBO, (c) LBO/g-CN, and (d) g-CN.

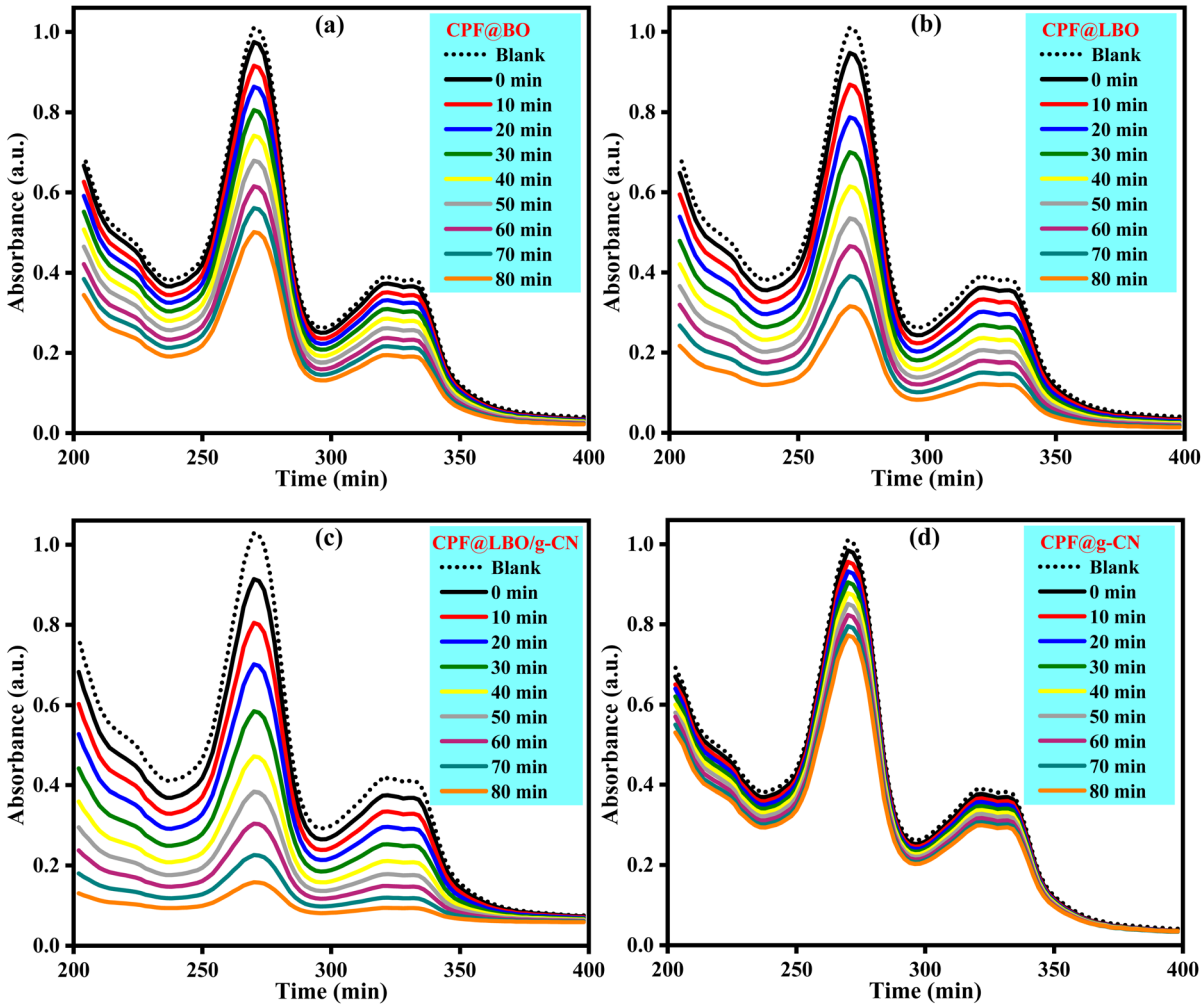


Fig. 7 UV-vis absorption (overlaid) of the samples separated from the aliquot during CPF photodegradation over defined time intervals in the presence of (a) BO, (b) LBO, (c) LBO/g-CN, and (d) g-CN.

calculated to be +2.30 V and +2.15 V for LBO and g-CN, respectively. Based on the band structure, the designed LBO/g-CN photocatalyst is diagrammatically presented in Fig. 5(d), showcasing improved charge separation due to hetero-structures assembling for the photocatalytic activity.

### 3.5 Photocatalytic performance

The as-designed photocatalysts, including BO, LBO, g-CN, and LBO/g-CN, were exposed to visible light to investigate their photocatalytic activity for MB and CPF degradation. The results for degrading the typically targeted pollutants were compared to reveal the impact of La-doping and heterojunction designing with the g-CN material.

**3.5.1 MB degradation.** MB was degraded in the presence of BO, LBO, g-CN, and LBO/g-CN photocatalysts. The absorbance spectra ($\lambda$ = 400–800 nm) of the samples separated from the aliquot at the defined time intervals (after every 10 minutes) are presented in Fig. 6(a–c). The MB degradation without the catalyst was negligible, as no decrease in MB concentrations was observed, which indicates that the MB is not prone to degrade under the same conditions without a photocatalyst. The decline in the absorption peak intensity at $\lambda_{max}$ showcases a decrease in the MB over time, which is more prominent for the heterojunction-based photocatalyst LBO/g-CN, highlighting its significant photocatalytic performance.

**3.5.2 CPF degradation.** CPF was degraded in the presence of as-designed catalysts to explore the photocatalytic performance and the non-specific pollutant degradation nature of the prepared photocatalyst. The absorption spectra ($\lambda$ = 400–800 nm) taken at different time intervals are overlaid and presented in Fig. 7(a–c). The sharp decline in CPF concentration in the presence of LBO/g-CN demonstrates the higher photocatalytic activity of the designed heterojunction.

**3.5.3 Kinetics of degradation.** The reaction kinetics of MB and CPF degradation were examined by applying the kinetics model, and the best fit was the 1st-order kinetics ($-\ln C_t/C_o$ *vs.* $t$) model as presented in Fig. 8(a and b).[69] The rate constant ($k$) was calculated from the slope of the linear fit of $-\ln C_t/C_o$ against time. The $k$ values for MB degradation in the presence of BO, LBO, and LBO/g-CN catalysts were 0.010 $min^{-1}$, 0.016 $min^{-1}$,

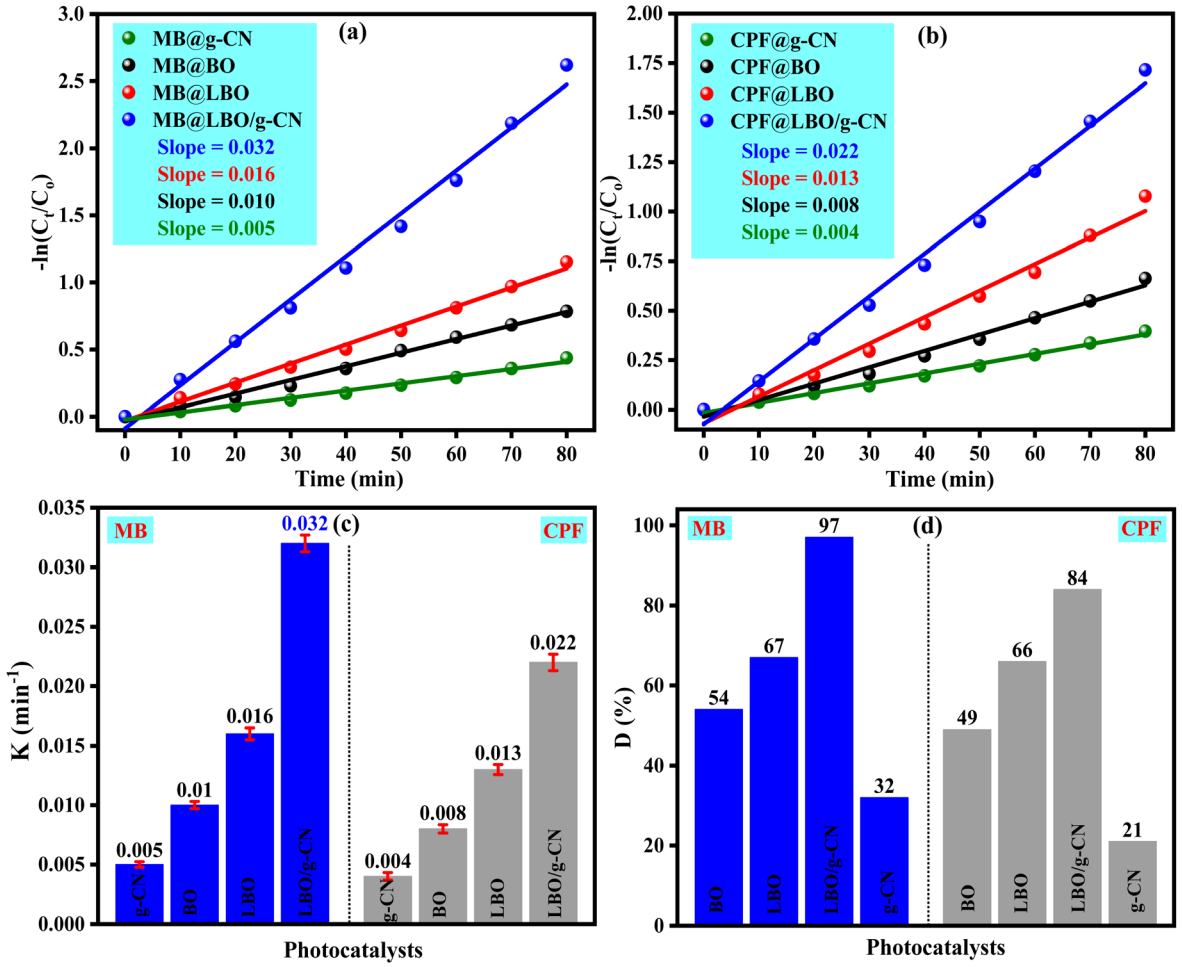


Fig. 8 (a and b) Kinetics study of MB and CPF degradation and (c and d) calculated rate constants and *D* (%) of MB and CPF over the g-CN, BO, LBO, and LBO/g-CN.

and 0.032 $min^{-1}$, while for CPF degradation, the rate constants were 0.008 $min^{-1}$, 0.013 $min^{-1}$, and 0.022 $min^{-1}$ in the presence of catalysts in a similar manner. The degradation (*D*, %) achieved for the targeted pollutants in the presence of BO, LBO, and LBO/g-CN catalysts was 54%, 67%, and 97% for MB, while CPF degraded to 49%, 66%, and 84%. The remarkable photocatalytic activity of the designed heterojunction LBO/g-CN for the degradation of both MB and CPF discloses its promising potential in the photocatalytic removal of organic pollutants. This improved efficiency can be attributed to the tuned optical response and prompt charge separation and transfer dynamics.

The detailed comparison of the present study with $Bi_2O_3$-based photocatalysts is summarized in tabular form to showcase the efficiency of LBO/g-CN (Table 1).

Table 1 Comparative analysis of present work with previous studies

| Sr. no. | Photocatalyst | Typical pollutant | Light source, catalyst dose, and pollutant concentration | Degradation (%)/time (min) | Reference |
|---|---|---|---|---|---|
| 1 | $CuO/Bi_2O_3$ | Rhodamine B | Visible-light, 35 mg, 10 ppm | 95.6%/180 min | 70 |
| 2 | $Ce\text{-}Bi_2O_3$ | Methyl orange | Visible-light, 1 g, 20 ppm | 83%/120 min | 71 |
| 3 | $Se\text{-}Bi_2O_3$ | Methylene blue | Visible-light, 0.05, 3.2 ppm | 88%/270 | 72 |
| 4 | $Au\text{-}Bi_2O_3$ | Rhodamine B | Visible-light, 1 g, 4.8 ppm | 80%/180 min | 73 |
| 5 | $Bi_2O_3$/biochar/g-$C_3N_4$ | Tetracycline | Visible-light, 0.06 g, 20 ppm | 86.7%/30 min | 74 |
| 6 | $Bi_2O_3$/activated carbon | Methyl orange | Visible-light, 0.2 g, 200 ppm | 72.5%/80 min | 75 |
| 7 | $Bi_2O_3$/MWCNTs | Cr(VI) | Visible-light, 1 g, 10 ppm | 87.48%/480 min | 76 |
| 8 | $Bi_2O_3$@g-$C_3N_4$ | Tetracycline | Visible-light, 0.5 g, 10 ppm | 80.2%/50 min | 77 |
| 9 | $La\text{-}Bi_2O_3$/g-$C_3N_4$ | Methylene blue/Ciprofloxacin | Visible light, 0.05 g, and 20 ppm | 97%/84%/80 min | Present study |

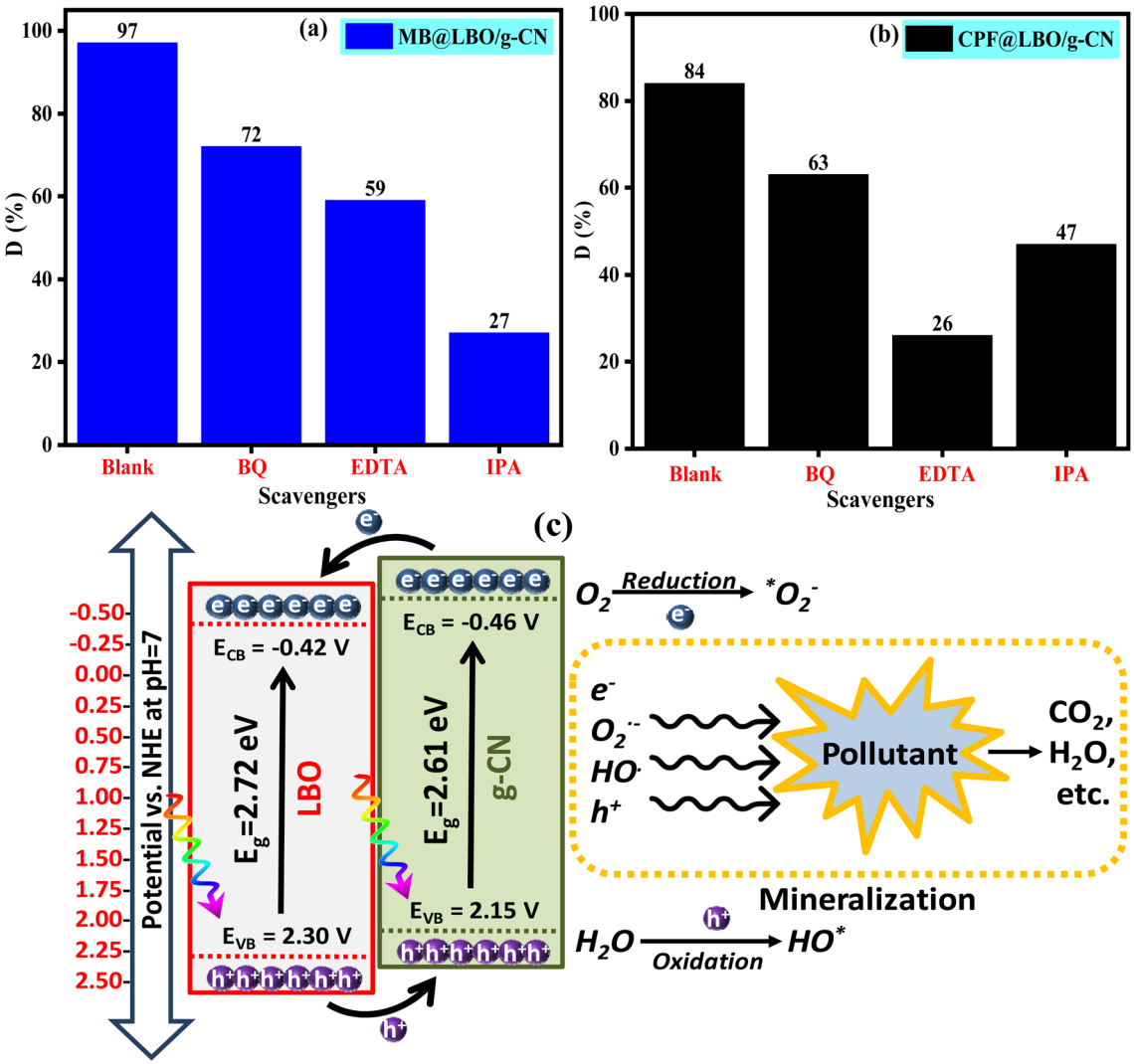


Fig. 9 (a) MB and (b) CPF degradation over catalyst LBO/g-CN along with scavengers, and (c) schematic display of degrading MB and CPF over the heterojunction LBO/g-CN.

**3.5.4 Proposed mechanism of MB and CPF degradation.** The photocatalytic MB and CPF degradation involve the production of reactive oxygen species, including superoxide radical anions ($*O_2^-$) and hydroxyl radicals (HO*) by the redox reaction of photo-separated charges, electrons in the conduction band, and holes in the valence band (electron–hole pair). Mechanistically, LBO/g-CN, under visible light exposure, undergoes electron excitation, and in turn, the electron is promoted to the conduction band $E_{CB}$ ($e^-$), generating holes in the valence band $E_{VB}$ ($h^+$). The slight difference in the $E_{CB}$ and $E_{VB}$ of the LBO and g-CN mitigates the recombination of separated charges by transferring and allowing these charge carriers to participate in a redox reaction, generating reactive oxygen species, which degrade the MB and CPF. The mechanism of MB and CPF degradation over LBO/g-CN catalyst is summarized in eqn (3)–(10).[78–82]

The production of these radical species and their relatively active involvement in MB and CPF degradation was tracked by scavenging investigation. The catalyst LBO/g-CN, along with scavengers, including IPA for hydroxide radicals quenching, EDTA for holes trapping, and benzoquinone for superoxide radical anions trapping,[83] were added to the MB/CPF solution, and the degradation achieved is presented in Fig. 9(a and b). The MB degraded to 72%, 59%, and 27%, while CPF showed 63%, 26%, and 47% degradation in the presence of BQ ($*O_2^-$ quencher), EDTA ($h^+$ quencher), and IPA (*OH quencher) over the catalyst LBO/g-CN.

$$\text{LBO/g-CN} + h\nu_{vis} \rightarrow \text{LBO/g-CN}\,[VB_{(h^+)} + CB_{(e^-)}] \quad (3)$$

$$\text{LBO/g-CN}\,[VB_{(h^+)} + CB_{(e^-)}] \rightarrow \text{LBO}\,[CB_{(e^-)}] + \text{g-CN}\,[VB_{(h^+)}] \quad (4)$$

$$VB_{(h^+)} + H_2O \rightarrow *OH + H^+ \quad (5)$$

$$CB_{(e^-)} + O_2 \rightarrow *O_2^- \quad (6)$$

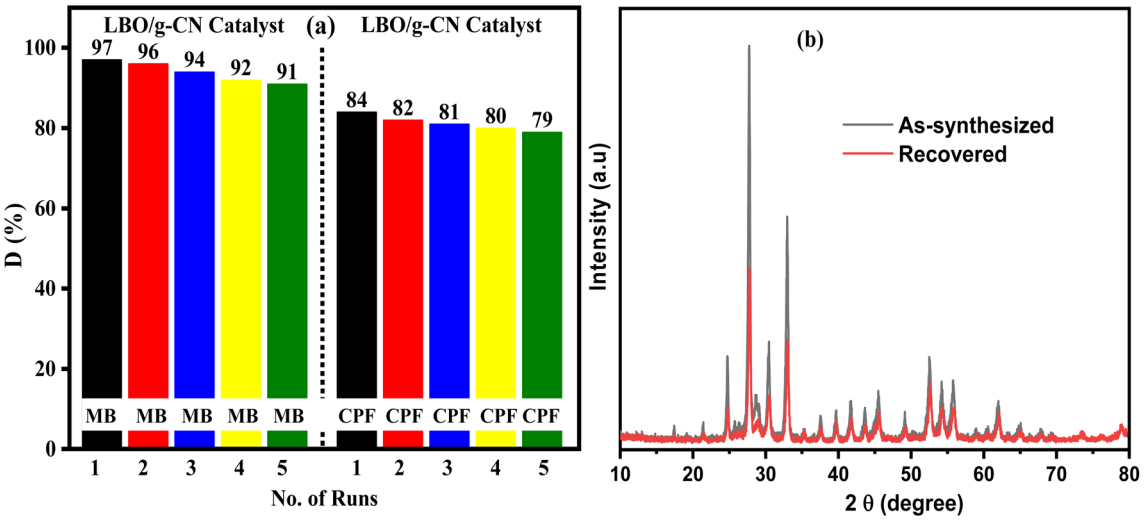


Fig. 10 (a) MB and CPF degradation (%) achieved during recycling of the LBO/g-CN catalyst and (b) diffraction pattern comparison of the as-synthesized and used photocatalyst to witness its stability.

$$*O_2^- + H^+ \rightarrow HOO* \quad (7)$$

$$HOO* + H_2O \rightarrow *OH \quad (8)$$

$$*O_2^-/*OH + CPF \rightarrow \text{Mineralized product} \quad (9)$$

$$*O_2^-/*OH + MB \rightarrow \text{Mineralized product} \quad (10)$$

**3.5.5 Reusability and stability.** The catalyst LBO/g-CN was recovered for MB and CPF degradation and reused to assess its stability and non-photocorrosive nature for practical applicability as a stable and reusable photocatalyst. After completing every cycle, the LBO/g-CN was recovered by centrifuging the aliquot after washing and oven drying before the subsequent cycle use. The catalyst features stability without relinquishing its efficiency (Fig. 10(a)), as the degradation (%) decrease was not substantial. The minor reduction in the efficiency can be attributed to catalyst dosage loss during its recovery or washing. After completing five cycles, the catalyst was recovered again, and stability was further explored by comparing the XRD patterns of the recovered catalyst to that of as-synthesized LBO/g-CN. No noticeable change was observed in the diffraction pattern of the recovered catalyst (Fig. 10(b)), which witnesses the stability of the designed heterojunction LBO/g-CN.

## 4. Conclusion

Pure bismuth oxide and its lanthanum-doped composition were fabricated by the economical and facile hydrothermal route, following the decoration of La-doped counterparts on g-CN by ultrasonication to assemble the heterojunction LBO/g-CN. XRD and FT-IR revealed the structural characteristics of the designed material, confirming the formation of BO, LBO, g-CN, and LBO/g-CN. The assembled LBO/g-CN exhibits excellent thermal stability, as witnessed by the TGA analysis. The SEM and TEM results revealed the decoration of LBO material over the 2D g-CN leaves. The band structure of bismuth oxide was tuned by La-doping, which red-shifted the absorption edge, featuring absorption in visible light. The electrochemical properties revealed prompt interfacial charge transfer and a lower recombination rate for the LBO/g-CN heterojunction, reflecting its promising potential for catalytic applications. The designed heterojunction LBO/g-CN shows significantly enhanced MB and CPF degradation compared to its non-assembled counterparts, disclosing its tuned optical activity and prompt interfacial charge transfer. In visible light irradiation for 80 minutes, MB and CPF degraded to 97% and 84%, following 1st-order kinetics. Scavenging studies disclose the significant contribution of reactive oxygen species, hydroxide radicals for MB, and holes in CPF degradation. The reusability of the LBO/g-CN catalyst without relinquishing its efficiency showcases its stability. The designed recoverable heterojunction LBO/g-CN with visible light activation and prompt interfacial charge transfer could be a promising photocatalyst for the photocatalytic degradation of toxic organic compounds.

## Author contributions

M. M. Rashed (project administration, methodology, funding acquisition, resources). Mohamed Abdel Rafea (data curation, conceptualization). Mohamed I. Attia (data curation, formal analysis). Mohamed R. El-Aassar (writing – original draft, data curation, formal analysis). Tasneem I. Hussein (conceptualization, validation). Salma Saddeek (validation, formal analysis). Imran Shakir (writing – review & editing). Mazen R. Alrahili (visualization). Muhammad Aadil (supervision).

## Conflicts of interest

There are no conflicts to declare.

## Data availability

Data will be available upon request.

## Acknowledgements

This work was supported and funded by the Deanship of Scientific Research at Imam Mohammad Ibn Saud Islamic University (IMSIU) (grant number IMSIU-DDRSP2602).

## References

1 V. Pasindu and I. Munaweera, Harnessing atomic-scale defect engineering in 2D photocatalysts: synergistic integration of nanocomposite architectures for bandgap tuning and charge transfer optimization, *RSC Adv.*, 2025, **15**, 34191–34210.

2 B. Abhishek, A. Jayarama, A. S. Rao, S. S. Nagarkar, A. Dutta, S. P. Duttagupta, S. S. Prabhu and R. Pinto, Challenges in photocatalytic hydrogen evolution: Importance of photocatalysts and photocatalytic reactors, *Int. J. Hydrogen Energy*, 2024, **81**, 1442–1466.

3 V. Arun, Y. D. Rahmayanti, L. Gnanasekaran, D. Shanmugapriya, T. M. Atmono, K. Khotimah, P. Vijayakumar, A. Rasool, A. Singh and M. Handayani, Z-Scheme Photocatalytic Mechanism in Inorganic-Organic rGO Mediated SnO2/CeTiO4 Nanocomposites for Efficient Degradation of Organic Pollutants, *J. Inorg. Organomet. Polym. Mater.*, 2026, 1–19.

4 H. K. Hakki and M. Sillanpää, Comprehensive analysis of photocatalytic and photoreactor challenges in photocatalytic wastewater treatment: A case study with ZnO photocatalyst, *Mater. Sci. Semicond. Process.*, 2024, **181**, 108592.

5 Y. Sari, P. L. Gareso, B. Armynah and D. Tahir, A review of TiO2 photocatalyst for organic degradation and sustainable hydrogen energy production, *Int. J. Hydrogen Energy*, 2024, **55**, 984–996.

6 B. Quy, N. Thu, V. Xuan, N. Hoa, N. Linh, V. Tung, V. Le, T. Thao, N. Ngan and P. Tho, Photocatalytic degradation performance of a chitosan/ZnO–Fe 3 O 4 nanocomposite over cationic and anionic dyes under visible-light irradiation, *RSC Adv.*, 2025, **15**, 1590–1603.

7 S. M. Albukhari, L. Al-Hajji and A. A. Ismail, Construction of nn heterojunction copper manganese spinel/mesoporous WO3 photocatalyst for efficient H2 evolution rate from aqueous glycerol, *Renewable Energy*, 2024, **228**, 120649.

8 S. Chi, Y. Tu, X. Li, J. Dang, T. Jin, D. Fang and J. Wang, Preparation of several Z-scheme CuBi2O4/Bi2O3 photocatalyst films loaded on different metal foils for efficient methylene blue degradation with synchronous hydrogen evolution, *Int. J. Hydrogen Energy*, 2024, **91**, 1009–1024.

9 J. Ma, J. Li, Z. Jiang, R. Zhang, T. Wu, C. Liu, L. Xu and Q. Feng, Hydrothermal preparation of a novel indium doped MoO3 photocatalyst with enhanced photocatalytic activity for Rhodamine B degradation, *Opt. Mater.*, 2024, **154**, 115792.

10 X. Zhu, C. Chen, Y. Shi, J. Wang, Y. Wang, L. Pan and Z. Guan, Dual-functional, highly efficient CaIn2S4/PDA@SnO2 photocatalyst with Z-Scheme for photocatalytic hydrogen production from water splitting and organic pollutant degradation, *J. Alloys Compd.*, 2024, **976**, 173151.

11 M. Kabir, M. Hossain, M. Jalil, S. Ghosh, M. Hossain, M. A. Ali, M. U. Khandaker, D. Jana, M. M. Rahman and M. Hossain, The efficacy of rare-earth doped V2O5 photocatalyst for removal of pollutants from industrial wastewater, *Opt. Mater.*, 2024, **147**, 114724.

12 L. Jie, X. Gao, X. Cao, S. Wu, X. Long, Q. Ma and J. Su, A review of CdS photocatalytic nanomaterials: Morphology, synthesis methods, and applications, *Mater. Sci. Semicond. Process.*, 2024, **176**, 108288.

13 J. A. S. Syed, Y. Huang, N. Han, J.-B. Fang, T.-Q. Zi and A.-D. Li, Magnetically separable Z-scheme ZnFe2O4/MoS2 photocatalyst for boosting photo-Fenton degradation activity by a hole-mediated mechanism, *J. Alloys Compd.*, 2024, **990**, 174508.

14 J. A. Khan, S. Ahamad, M. A. H. Ansari, M. Tauqeer, C.-H. Park, J. P. Park, C.-H. Choi and A. Mohammad, State-of-the-art in ZnS-based nanoarchitects for visible-light photocatalytic degradation of antibiotics and organic dyes, *J. Water Process Eng.*, 2024, **67**, 106151.

15 R. Rajendran, O. Rojviroon, P. Arumugam, K. Natchimuthu, V. Vasudevan, J. Kannupaiyan, R. Muangmora, P. Phouheuanghong and T. Rojviroon, Design and fabrication of g-C3N4/Bi2S3 heterojunction photocatalysts for efficient organic pollutant degradation and antibacterial activity, *J. Alloys Compd.*, 2024, **976**, 173116.

16 S. R. Mishra, V. Gadore and M. Ahmaruzzaman, Shining light on sustainable and clean hydrogen production: recent developments with In2S3 photocatalysts, *Nano Energy*, 2024, 109820.

17 X. Wang, Y. Zhang, S. Jiang, J. Su and S. Song, Localized CdS homojunctions with optimal ratio of high and low index facets to dynamically boost H2O splitting into H2 energy, *J. Mater. Sci. Technol.*, 2024, **171**, 94–100.

18 Q. Yang, J. Wei, S. Li and Y. He, Fabrication of Z-scheme ZnIn2S4/ZnSe heterostructed microspheres toward antibiotic degradation from real pharmaceutical wastewater, *Opt. Mater.*, 2024, **155**, 115905.

19 E. A. Alabdullkarem and J. Khan, Dual-function gC 3 N 4 anchored Cu–ZnS hybrid nanostructures for sustainable energy storage and environmental remediation, *RSC Adv.*, 2025, **15**, 23801–23818.

20 M. D. Khan, I. Fareed, M. F. Khan, Z. U. Rehman, U. Ayoub, A. Ahmed and F. K. Butt, Novel N-doped ZnO and O-doped g-$C_3N_4$ heterojunction: Enhanced photocatalytic degradation and robust electrochemical biosensing of ascorbic acid, *Diamond Relat. Mater.*, 2025, **151**, 111752.

21 Q. Zhou, Z. Liu, X. Wang, Y. Li, X. Qin, L. Guo, L. Zhou and W. Xu, Co3S4-pyrolysis lotus fiber flexible textile as a hybrid electrocatalyst for overall water splitting, *J. Energy Chem.*, 2024, **89**, 336–344.

22 N. R. Barveen, B. Parasuraman, P.-Y. Wang, C.-W. Zeng, Y.-W. Cheng and P. Thangavelu, Facile construction of ZnWO4/g-C3N4 heterojunction for the improved photocatalytic degradation of MB, RhB and mixed dyes, *Surf. Interfaces*, 2024, **53**, 105039.
23 M. Saeed, H. Asghar, I. Khan, N. Akram and M. Usman, Synthesis of TiO2-g-C3N4 for efficient photocatalytic degradation of Congo Red dye, *Catal. Today*, 2025, **447**, 115154.
24 R. Song, L. Yao, C. Sun, D. Yu, H. Lin, G. Li, Z. Lian, S. Zhuang and D. Zhang, Electrospun membranes anchored with g-C3N4/MoS2 for highly efficient photocatalytic degradation of aflatoxin B1 under visible light, *Toxins*, 2023, **15**, 133.
25 D. Ma, J. Tang, G. He, Y. Xue, S. Pan, F. Liu and J. Zhao, Enhancing photocatalytic degradation of rhodamine B with visible-light-driven HCl-assisted Bi2O3 photocatalysts: activity, mechanism, and pathways, *Mater. Sci. Semicond. Process.*, 2024, **181**, 108672.
26 A. Jaison, H. U. Lee, J. Hur, A. Mohan and Y.-C. Lee, Facile synthesis of Ni-doped tetrahedral γ-Bi2O3 and selective photocatalytic degradation of Congo red under simulated sunlight, *J. Alloys Compd.*, 2024, **1004**, 175727.
27 X. Wang, C. Du, Y. Yu, W. Li, T. Li, S. Wang, S. Mao, Y. Wang, J. Zhao and C. Xiong, Efficient photocatalytic degradation with a lattice-matched α-Bi2O3/Co3O4 Z-scheme heterojunction: An integrated experimental and DFT study, *J. Water Process Eng.*, 2024, **65**, 105829.
28 F. Li, G. Liu, M. Liu, X. Liu, L. Dong, D. Wang, Y. Huang, J. Zhang, Z. Yang and W. Yang, Oxygen vacancies enriched Z-scheme BiOI/Bi2O3 heterojunction with controllable band-gap for dye degradation and Cr (VI) reduction, *Ceram. Int.*, 2025, **51**, 8647–8657.
29 M. Jahed-Jaafargolikhanlo, A. Habibi-Yangjeh, K. Pournemati and A. Khataee, One-pot anchoring BaBi2O6/Bi2O3 nanoparticles on oxygen vacancy rich TiO2: Double Z-scheme nanocomposites with QDs size for elimination of wastewater pollutants, *Adv. Powder Technol.*, 2024, **35**, 104542.
30 R. Boudraa, D. Talantikite-Touati, A. Djermoune, A. Souici, M. Kebir, F. Ait Merzeg, A. Amrane, J.-C. Bollinger and L. Mouni, Comprehensive characterization and unprecedented photocatalytic efficacy of TiO2-CuO-La2O3 and TiO2-CuO-Bi2O3 nanocomposites: A novel approach to environmental remediation, *Mater. Sci. Eng., B*, 2025, **312**, 117863.
31 J. Wang, P. Ren, X. Zhao, Z. Chen, Y. Jin and Z. Zhang, Acid-alkali assisted synthesis of white tremella-like g-C3N4 homojunction for photocatalytic degradation under visible light, *Mater. Res. Bull.*, 2024, **171**, 112619.
32 Y. Lu, Y. Zhao, S. Wang and B. Hu, Exploring charge-transfer of 2D borophene in carbon nitride: boosting uranium photoreduction, *Desalination*, 2025, 119488.
33 M. R. Alrahili, M. A. Rafea, M. E. Zaki, M. Khairy, M. R. El-Aassar, S. Albarakati, I. Shakir, A. K. Alanazi and M. Aadil, Rationally designed In–CeO 2/gC 3 N 4 S-scheme heterojunction photocatalyst with tuned redox ability for the photocatalytic degradation of pharmaceutical contaminants, *RSC Adv.*, 2025, **15**, 47271–47281.
34 J. Pei, H. Li, D. Yu and D. Zhang, g-C3N4-based heterojunction for enhanced photocatalytic performance: a review of fabrications, applications, and perspectives, *Catalysts*, 2024, **14**, 825.
35 J. Pei, H. Li, S. Zhuang, D. Zhang and D. Yu, Recent Advances in g-C3N4 Photocatalysts: A Review of Reaction Parameters, Structure Design and Exfoliation Methods, *Catalysts*, 2023, 1402.
36 H. Wang, X. Li, D. Yang, C. Chen, Y. Duan, J. Wang and W. Guo, Heteroatom atom modified g-C3N4/Bi2MoO6 Z-scheme for enhanced photocatalytic performance, *Appl. Surf. Sci.*, 2025, **687**, 162246.
37 J. Y. Lu, Z. Q. Bu, Y. Q. Lei, D. Wang, B. He, J. Wang and W. T. Huang, Facile microwave-assisted synthesis of Sb2O3-CuO nanocomposites for catalytic degradation of p-nitrophenol, *J. Mol. Liq.*, 2024, **409**, 125503.
38 T. Zahra, M. M. Alanazi, S. A. Abdelmohsen, S. D. Alahmari, M. Abdullah, S. Aman, A. Dahshan, A. Henaish, Z. Ahmad and H. M. T. Farid, Fabrication of MnAl2O4/g-CN nanohybrid as an advantageous electrode for supercapacitor applications, *Ceram. Int.*, 2024, **50**, 14469–14479.
39 K. El Akeb, H. Bessaha, H. Aguedal, M. Bouraada, B. Azambre and M. E. A. E. Elmeliani, BiTi-oxides semiconductor: Advanced UV and solar photocatalysts for the aqueous oxidation of organic pollutants rhodamine B and crystal violet, *J. Water Process Eng.*, 2024, **65**, 105866.
40 A. Gandamalla, S. Manchala, A. Verma, Y.-P. Fu and V. Shanker, Development of highly efficient Ce (MoO4) 2/g-C3N4 composite for the photocatalytic degradation of methylene blue and ciprofloxacin under visible light, *J. Mol. Struct.*, 2024, **1297**, 136896.
41 A. Rasheed, M. E. El Sayed, S. Yousaf, A. Samir, M. F. Warsi and Z. M. El-Bahy, Fluorine-doped cobalt ferrite integrated into 2D MXene with extended solar spectrum response and boosted charge separation for the removal of recalcitrant organic pollutants, *Results Phys.*, 2024, **67**, 108049.
42 A. Badawi, M. Althobaiti, E. E. Ali, S. S. Alharthi and A. N. Alharbi, A comparative study of the structural and optical properties of transition metals (M= Fe, Co, Mn, Ni) doped ZnO films deposited by spray-pyrolysis technique for optoelectronic applications, *Opt. Mater.*, 2022, **124**, 112055.
43 H. Chen, Y. Zhu, J. Wu, M. Peng, S. Deng, H. Yang and J. Yang, Cu-doped ZnCdS-based photocatalyst for efficient photocatalytic hydrogen production by photothermal assistance, *Case Stud. Therm. Eng.*, 2024, **61**, 104970.
44 A. Rasheed, I. Bibi, F. Majid, S. Kamal, B. Taj, M. Raza, N. Khaliq, K. M. Katubi, S. Ezzine and N. Alwadai, Mn doped SrFe12O19 fabricated via facile microemulsion route and solar-light-driven photocatalytic removal of crystal violet dye, *Phys. B*, 2022, **646**, 414303.
45 V. Venkatachalam, S. Ganapathy, I. Perumal and M. Anandhan, Crystal shape and size of CdTe colloidal quantum dots controlled by silver doping for enhanced

quantum dots sensitized solar cells performance, *Colloids Surf., A*, 2023, **656**, 130296.

46 S. Ibrahim, A. Ali and A. M. Fathi, A comprehensive investigation of Bi2O3 on the physical, structural, optical, and electrical properties of K2O. ZnO. V2O5. B2O3 glasses, *Sci. Rep.*, 2024, **14**, 8518.

47 A. Alruwaili and A. M. El Sayed, Characterization and the physical properties of nano-sized Bi2O3/polymer for energy and high-refractive index applications, *Results Phys.*, 2024, **61**, 107746.

48 I. Saber, K. Dahmani, M. Galai, A. E. Magri, R. Hsissou, H. Barbita, M. Belfaquir, I. Warad, N. AL-Zaqri and M. Elyoubi, Synthesis and characterization of new eco-friendly vitreous system Bi2O3–B2O3–BaO: Structural, morphologic, and thermal analysis, *Opt. Mater.*, 2024, **149**, 115079.

49 M. Devi, S. Upadhyay, R. A. Mir, N. Kumar and S. Sharma, Synthetic waste derived graphitic carbon nitride (g-CN) and g-CN/carbon hybrid for supercapacitors, *J. Energy Storage*, 2023, **73**, 109067.

50 H. Yuan, H. Sun, Y. Shi, J. Wang, A. Bian, Y. Hu, F. Guo, W. Shi, X. Du and Z. Kang, Cooperation of carbon doping and carbon loading boosts photocatalytic activity by the optimum photo-induced electron trapping and interfacial charge transfer, *Chem. Eng. J.*, 2023, **472**, 144654.

51 K. Zafar, M. Aadil, M. N. Shahi, H. Sabeeh, M. F. Nazar, M. Iqbal and M. A. Yousuf, Physical, structural and dielectric parameters evaluation of new Mg1-x Cox NiyFe2-yO4 nano-ferrites synthesized via wet chemical approach, *AAAFM Energy*, 2020, **1**, 36–44.

52 M. Sabir, M. Ramzan, M. Imran, S. R. Ejaz, A. Anwar, S. Ahmad, M. Aamir and M. Aadil, Synthesis of La1-xGdxFe1-yCoyO3/r-GO nanocomposite with integrated features for the treatment of hazardous industrial effluents, *Ceram. Int.*, 2022, **48**, 9134–9145.

53 L. Harikrishnan and A. Rajaram, Constructive Z-scheme interfacial charge transfer of a spinel ferrite-supported g-C3N4 heterojunction architect for photocatalytic degradation, *J. Alloys Compd.*, 2024, **976**, 172987.

54 A. W. Alrowaily, B. Alotaibi, M. Ali, H. A. Alyousef, M. F. Alotiby, M. Abdullah, A. G. Al-Sehemi, A. Henaish, Z. Ahmad and S. Aman, One step hydrothermal preparation of NiFe2O4@ g-CN nanosheets for low-cost electrode material storage devices, *J. Mater. Sci.: Mater. Electron.*, 2024, **35**, 608.

55 T. Zahra, M. M. Alanazi, A. Gassoumi, S. A. Abdelmohsen, M. Abdullah, S. Aman, A. Henaish and H. M. T. Farid, High-performance MoO3/g-CN supercapacitor electrode material utilizing MoO3 nanoparticles grafted on g-CN nanosheets, *Diamond Relat. Mater.*, 2024, **143**, 110892.

56 U. E. Romman, I. Shakir, I. A. Shaaban, M. A. Assiri, K. Chaudhary, M. F. Warsi and M. Shahid, Silver-doped lanthanum nickel oxide decorated Ti3C2Tx MXene nanocomposite (Ag–LaNiO3/MXene) for advanced photocatalytic waste-water treatment, *Opt. Mater.*, 2024, **147**, 114678.

57 I. Ayman, M. Aadil, M. Shahid, A. Khalid, H. Samama, H. Somaily, M. F. Warsi and R. M. Mohamed, Wet synthesis of magnetically retrievable Mn/Nd co-doped cobalt ferrites for visible light-driven photocatalytic annihilation of azo dye, *Mater. Sci. Semicond. Process.*, 2024, **178**, 108462.

58 M. Hussain, M. Mahmoud, A. Rasheed, I. H. El Azab, M. Anwar and Z. M. El-Bahy, Silver-doped cadmium aluminate and its MXene based composite for visible-light driven photocatalytic degradation of organic pollutants, *Opt. Mater.*, 2024, **155**, 115824.

59 B. Wang, X. Feng, Y. Liu, X. Wang, E. Liu, Y. Zhao, Z. Miao and Z. Li, Ultrafast Electron Transfer Coupled with a Proton Relay in an Anisotropic Dual S-Scheme Heterojunction for Overcoming Kinetics Mismatch in H2O2 Photosynthesis, *Adv. Sci.*, 2025, e22285.

60 R. Song, S. Kang, L. Yao, L. Zheng, D. Yu and D. Zhang, Construction of an La-BiVO4/O-doped g-C3N4 heterojunction photocatalyst embedded in electrospinning nanofibers, *Langmuir*, 2023, **39**, 6647–6656.

61 B. Huwaimel, K. M. Younes, A. S. Abouzied, S. A. Almahmoud, S. Alshehri, Z. M. El-Bahy and M. F. Warsi, Cerium-doped indium vanadate microspheres loaded onto the 2D conductive matrix for boosted photodegradation of persistent organic pollutants, *Ceram. Int.*, 2025, **51**(10), 12806–12817.

62 H. Somaily, Tailoring the electrical, optical, physical, and photocatalytic properties of indium-doped cerium molybdate microstructures reinforced with a 2D carbonaceous, *Ceram. Int.*, 2024, **50**, 36717–36730.

63 J. Louis, N. T. Padmanabhan, M. K. Jayaraj and H. John, Exploring enhanced interfacial charge separation in ZnO/reduced graphene oxide hybrids on alkaline photoelectrochemical water splitting and photocatalytic pollutant degradation, *Mater. Res. Bull.*, 2024, **169**, 112542.

64 X. Wang, Z. Gao, X. Gao, P. Song, Z. Sun and Z. Jin, Recent advances and optoelectronic applications of Cu–Ag–Bi–I quaternary lead-free perovskites, *Semicond. Sci. Technol.*, 2025, **40**, 043002.

65 S. Pahi, B. Mahapatra, A. Behera, S. K. Singh and R. K. Patel, Fermi level induced band edge alignment and band bending in Ag3PO4/Cu2O pn heterojunction for proficient photocatalytic applications, *Mater. Chem. Phys.*, 2023, **305**, 127992.

66 Q. Qin, T. Xiao and X. Zhu, Fabrication of Bi2O3/In2O3 pn heterojunction with enhanced photocatalytic activity by efficient interfacial charge transfer, *J. Saudi Chem. Soc.*, 2024, **28**, 101919.

67 Z. Ahmad, A. Khalid, Z. M. Aldhafeeri, I. Barsoum, E. G. Hanna, M. Hasan, A. Anwar and M. Aadil, Fine-tuning of redox-ability, optical, and electrical properties of Bi2MoO6 ceramics via lanthanide doping and rGO integration for photo-degradation of Methylene Blue and Ciprofloxacin, *J. Alloys Compd.*, 2024, **1002**, 175466.

68 P. Lu, Y. Peng, Y. Yang, S. Chen, J. Shang, C. Yang, M. Xu, J. Bai, Z. Zhao and X. Hu, Visible-light-driven photocatalytic for degrading tetracycline wastewater by BiOI/Bi2O3 Z-scheme heterojunction, *J. Environ. Chem. Eng.*, 2024, **12**, 114395.

69 K. M. Katubi, A. Rasheed, A. Ihsan, B. Shaheen, Z. Alrowaili, M. Al-Buriahi, M. I. Din, I. Shakir and S. Munir, Neodymium-doped nickel cobaltite reinforced with 2D MXene nanocomposite (Nd-NiCo2O4/MXene) for enhanced photocatalytic degradation of the organic pollutants, *Opt. Mater.*, 2024, **152**, 115390.

70 A. Negash, L. M. Derseh, A. Tedla and J. M. Yassin, Eco-friendly synthesis of CuO/Bi2O3 nanocomposite for efficient photocatalytic degradation of rhodamine B dye, *Sci. Rep.*, 2024, **14**, 23393.

71 S. Wu, J. Fang, X. Xu, Z. Liu, X. Zhu and W. Xu, Microemulsion synthesis, characterization of highly visible light responsive rare earth-doped Bi2O3, *Photochem. Photobiol.*, 2012, **88**, 1205–1210.

72 R. Sharma, M. Khanuja, S. N. Sharma and O. P. Sinha, Reduced band gap & charge recombination rate in Se doped α-Bi2O3 leads to enhanced photoelectrochemical and photocatalytic performance: theoretical & experimental insight, *Int. J. Hydrogen Energy*, 2017, **42**, 20638–20648.

73 H.-Y. Jiang, K. Cheng and J. Lin, Crystalline metallic Au nanoparticle-loaded α-Bi 2 O 3 microrods for improved photocatalysis, *Phys. Chem. Chem. Phys.*, 2012, **14**, 12114–12121.

74 L. Huang, H. Liu, Y. Wang, T. C. Zhang and S. Yuan, Construction of ternary Bi2O3/biochar/g-C3N4 heterojunction to accelerate photoinduced carrier separation for enhanced tetracycline photodegradation, *Appl. Surf. Sci.*, 2023, **616**, 156509.

75 P. Zhang, L. Yin, X. Yang, J. Wang, M. Chi and J. Qiu, Cotton-derived 3D carbon fiber aerogel to in situ support Bi2O3 nanoparticles as a separation-free photocatalyst for antibiotic removal, *Carbon*, 2023, **201**, 110–119.

76 P. Radhakrishnan and A. Sivasamy, Photocatalytic reduction of chromium (VI) using multiwall carbon nanotubes/bismuth oxide nanocomposite under solar irradiation, *Environ. Sci. Pollut. Res.*, 2024, **31**, 4747–4763.

77 Y. Hong, C. Li, B. Yin, D. Li, Z. Zhang, B. Mao, W. Fan, W. Gu and W. Shi, Promoting visible-light-induced photocatalytic degradation of tetracycline by an efficient and stable beta-Bi2O3@ g-C3N4 core/shell nanocomposite, *Chem. Eng. J.*, 2018, **338**, 137–146.

78 S. M. Hossain, L. Tijing, N. Suzuki, A. Fujishima, J.-H. Kim and H. K. Shon, Visible light activation of photocatalysts formed from the heterojunction of sludge-generated TiO2 and g-CN towards NO removal, *J. Hazard. Mater.*, 2022, **422**, 126919.

79 S. Iqbal, J. Liu, H. Ma, W. Liu, S. Zuo, Y. Yu, N. Yan and M. A. Mushtaq, Synergistic photocatalytic performance of Fe@ Fe2O3 core-shell nanostructures supported on g-C3N4 nanosheets for RhB and phenol decolorization: Fabrication, characterization, and mechanistic insights, *J. Water Process Eng.*, 2023, **53**, 103866.

80 Z. Ajmal, A. Hayat, M. Qasim, A. Kumar, A. El Jery, W. Abbas, M. B. Hussain, A. Qadeer, S. Iqbal and S. Bashir, Assembly of a novel Fe2TiO5-impregnated donor-π-acceptor conjugated carbon nitride for highly efficient solar water splitting, *Sustainable Mater.Technol.*, 2023, **36**, e00594.

81 G. Tian, Z. Li, C. Zhang, X. Liu, X. Fan, K. Shen, H. Meng, N. Wang, H. Xiong and M. Zhao, Upgrading CO2 to sustainable aromatics via perovskite-mediated tandem catalysis, *Nat. Commun.*, 2024, **15**, 3037.

82 X. Yang, Y. Xie, X. Zheng, Y. Zhao, Q. Zhang and H. Yan, Novel design and fabrication of Bi2S3@ NC nanofibers as promising anodes for advanced potassium energy storage, *Electrochim. Acta*, 2025, 148045.

83 K. Shanthini and V. Manivannan, Mechanochemical Synthesis of GCN/Nb2O5/Bi2O3Ternary Composite Photocatalyst for Enhanced Visible Light Driven Degradation of Organic Pollutants, *J. Inorg. Organomet. Polym. Mater.*, 2025, **35**, 6366–6376.